Remote Sensing of Environment 326 (2025) 114765

Contents lists available at ScienceDirect

Remote Sensing of Environment

journal homepage: www.elsevier.com/locate/rse

# Spatial and temporal variability of surface deformation in a paraglacial alpine environment measured from satellite radars

Nicolas Oestreicher [a,b,c,d,*], Andrea Manconi [a,c,d], Clément Roques [e], Adriano Gualandi [f,g], Simon Loew [a]

[a] Department of Earth Sciences, ETH Zürich, Sonneggstrasse 5, Zürich, 8092, Switzerland
[b] University of Geneva, Department of Earth Sciences, Geneva, Switzerland
[c] WSL Institute for Snow and Avalanche Research SLF, Davos Dorf, Davos, Switzerland
[d] Climate Change, Extremes and Natural Hazards in Alpine Regions Centre CERC, Davos Dorf, Davos, Switzerland
[e] Centre for Hydrogeology and Geothermics (CHYN), University of Neuchâtel, Neuchâtel, Switzerland
[f] University of Cambridge, Department of Earth Sciences, Bullard Laboratories, Cambridge, United Kingdom
[g] Istituto Nazionale di Geofisica e Vulcanologia (INGV), Osservatorio Nazionale Terremoti (ONT), Roma, Italy

ARTICLE INFO

Edited by Jing M. Chen

Dataset link: https://doi.org/10.3929/ethz-b-000563187, https://doi.org/10.3929/ethz-b-000701944, http://doi.org/10.5281/zenodo.4322548

*Keywords:*
Surface deformation
Groundwater
Glacier retreat
Paraglacial
Alps

ABSTRACT

Using satellite radar interferometry, we investigate surface deformation in the Great Aletsch Glacier region from 2015 to 2021. By applying a statistical blind source separation method on displacement timeseries, our study reveals irreversible trends near large slope instabilities, potentially indicating slope responses to the glacier's retreat. Moreover, annual cyclic deformation indicates significant pore pressure variations in fractured bedrock slopes resulting from groundwater storage and discharge processes. These spatial variations, assessed with satellite radars, reflect changes in pore pressure and rock mass hydromechanical properties, aligning with continuous ground monitoring data. This study demonstrates the potential of using satellite interferometry to investigate slope-scale mechanical processes driven by seasonal to multiannual environmental factors in complex alpine regions. It is the first timeseries synthetic aperture radar (TS-InSAR) study in a paraglacial environment validated by spatially distributed, high-resolution ground monitoring data. Moreover, it shows the advantages of the TS-InSAR high spatial coverage and its capacity to complement ground monitoring during data interruptions at ground stations. Combining satellite data with ground-based measurements and coherent structural hypotheses opens new possibilities for studying similarly remote and less instrumented regions.

## 1. Introduction

Ground deformation in alpine environments results from multiple tectonic and environmental factors (Sternai et al., 2019) and can inform us about processes happening at and below the surface, such as tectonic activity (Bock et al., 1993), gravitational instabilities (Agliardi et al., 2020), changes in surface loads (Mey et al., 2016), thermoelasticity of the subsurface (Collins et al., 2018), as well as poroelastic changes in aquifers (Loew et al., 2007; Vasco et al., 2019). Due to the amplified effects of climate change (Huss and Hock, 2018), deglaciation is progressively exposing large areas (Oliva et al., 2020) to potential slope instabilities. Failure can occur shortly after the glacier retreats or with delay due to the progressive accumulation of damage (Ballantyne et al., 2014; Grämiger et al., 2020). In this context, information on the evolution of the surface deformation of such areas is critical to understanding better where new slope instabilities could develop and how environmental factors could influence their formation.

Measuring ground displacements at relevant spatial (e.g., daily) and temporal (e.g., centimetric) resolutions is challenging in alpine environments, mainly because of costs associated with deploying monitoring systems and the difficulties of accessing remote and hazardous places. Remote sensing has increased our capability to gain quantitative insights into the properties and kinematics of land surfaces globally. Among other methods, the continuous development of the Time-Series Interferometric Synthetic Aperture Radar (TS-InSAR) in the past decades allowed quantification of the ground motion (Rosen et al., 2000; Crosetto et al., 2016; Chen et al., 2012). Noteworthy, several recent examples have shown the capability of TS-InSAR to monitor movement related to changes in groundwater storage in different geographic settings (Béjar-Pizarro et al., 2017; Neely et al., 2021; Ali et al., 2022; Song et al., 2022). Applying TS-InSAR might be challenging in mountain environments because of the intrinsic limitations associated

* Corresponding author at: WSL Institute for Snow and Avalanche Research SLF, Davos Dorf, Davos, Switzerland.
*E-mail address:* nicolas.oestreicher@slf.ch (N. Oestreicher).

https://doi.org/10.1016/j.rse.2025.114765
Received 5 November 2024; Received in revised form 10 March 2025; Accepted 11 April 2025
Available online 7 May 2025
0034-4257/© 2025 The Authors. Published by Elsevier Inc. This is an open access article under the CC BY license (http://creativecommons.org/licenses/by/4.0/).

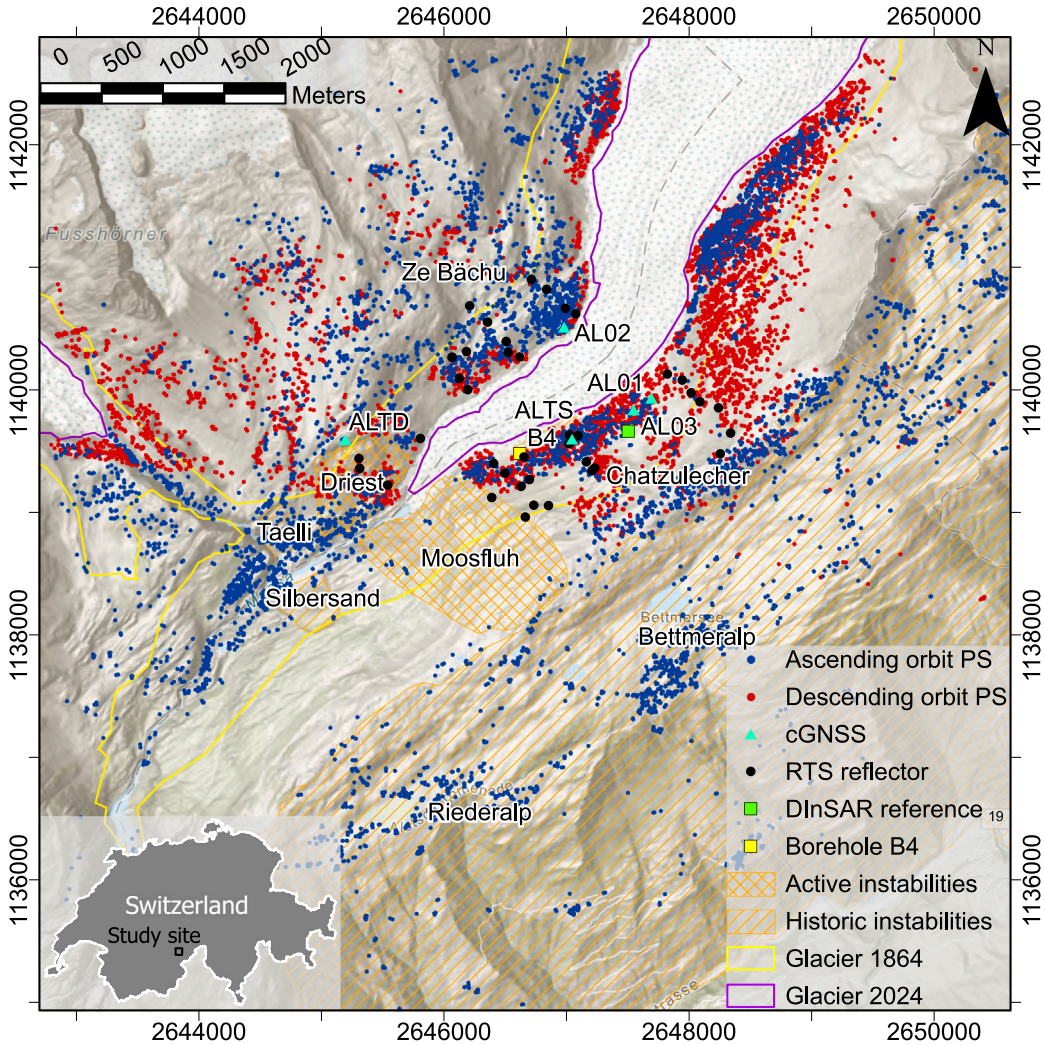


**Fig. 1.** Study area with selected Persistent Scatterers (PS) for the analysis of the ascending (blue) and descending (red) orbits and the TS-InSAR unwrapping reference point (green rectangle). cGNSS stations (cyan triangles), RTS reflectors (black points), and the borehole (yellow square) used in this study are drawn around the tongue of the Great Aletsch glacier, close to a range of large instabilities (orange patches). The glacier extent in 1864 is drawn from the Dufour map (Dufour, 1865), and in 2024, it is derived from the orthophotograph (Federal Office of Topography swisstopo, 2024). The location of the study area in Switzerland is shown in the bottom left corner. (For interpretation of the references to color in this figure legend, the reader is referred to the web version of this article.)

with snow cover, geometric distortions (layover and shadowing), and atmospheric phase screen (Wasowski and Bovenga, 2014; Manconi, 2021). It is possible to overcome such issues with more satellite orbits or different methods and by restricting monitoring to snow-free periods or reducing the number of monitored points (Strozzi et al., 2017; Manconi et al., 2024; Chen et al., 2025). The relatively low amplitude of expected seasonal deformation (centimetric) also challenges the use of TS-InSAR. However, with the new satellite data available and by applying modern processing approaches and signal decomposition techniques, we show that TS-InSAR can reveal key quantitative insights about surface displacement dynamics associated with mountain slope instabilities.

We use surface displacements measured with TS-InSAR in the Aletsch Valley, Switzerland (see Fig. 1). This region is intensively studied as it hosts the current longest European Alps glacier that retreated over 1 km in length between 2000 and 2020 (GLAMOS - Glacier Monitoring Switzerland, 2021). The bedrock in the area is composed of strongly foliated gneisses and granite from the Aar massif (Berger et al., 2016). Several instabilities are identified around the glacier tongue (Strozzi et al., 2010; Kos et al., 2016; Glueer et al., 2019; Hugentobler et al., 2020), some being inactive, while others are moving at rates high enough to influence and interact with the glacier flow (Storni et al., 2020). It is essential to efficiently monitor surface deformation in the region because of the large-scale paraglacial environment, hazards associated with slope instabilities and rapid glacier retreat. The glacier might pass its Holocene minimum level in the coming decades, and it could induce an increase in the number and size of paraglacial slope deformations (Grämiger et al., 2017).

A large monitoring setup (see Fig. 1) was installed in the Aletsch Valley in 2013 and has improved since with Robotic Total Stations (RTS) and continuous Global Navigation Satellite Systems stations (cGNSS) (Frukacz et al., 2017; Glueer et al., 2021). With extensive fieldwork, the system helped characterize the structures and kinematic model of the Moosfluh landslide (Glueer et al., 2020). The objectives of the monitoring network extend beyond the surveillance of the major instabilities and include the study of long-term progressive slope damage, landslide formation in glacial and para-glacial environments, hydro-mechanical landslide-glacier interactions and monitoring system development (Frukacz et al., 2017; Grämiger et al., 2017, 2018; Manconi et al., 2018; Glueer et al., 2019, 2020; Hugentobler et al., 2020; Storni et al., 2020; Grämiger et al., 2020; Hugentobler et al., 2021; Oestreicher et al., 2021; Glueer et al., 2021; Oestreicher et al., 2023). To increase the spatial and temporal coverage of the observations of ground deformation, we have processed the available data acquired

from the ESA Sentinel-1 constellation (Torres et al., 2012) in the period 2015–2021. We generated surface velocity maps and displacement time series with the interferometric point target analysis (IPTA) (Werner et al., 2003). We selected IPTA as part of the Persistent Scatterers Interferometry category of algorithms because we expected to recognize only some scatterers that would be reliable enough for this analysis. The IPTA results have been further exploited using an advanced signal decomposition method to explain different spatial and temporal patterns of the measured deformation signal and identify their relationship with environmental controlling factors (Gualandi and Liu, 2021). We finally validated the TS-InSAR data analysis outcomes with ground-truth data and previous site knowledge (Hugentobler et al., 2020; Grämiger et al., 2020; Oestreicher et al., 2021, 2023) and extended the spatio-temporal analysis of ongoing slope displacement processes into formerly unexplored regions in the lower Aletsch valley study area. This is the first study using TS-InSAR of the valley near the glacier tongue area extending to slopes generally considered stable and the first validation of TS-InSAR with spatially distributed high-resolution ground monitoring in a paraglacial environment.

## 2. Methods

### 2.1. Time-Series Interferometric Synthetic Aperture Radar (TS-InSAR) data

We considered the ESA Sentinel-1 imagery acquired during the period 2015–2021. A total of 329 images from the Track 15, Ascending orbit (hereafter T015 A) and 346 from the Track 66, Descending orbit (hereafter T066D), were selected, and processed with the GAMMA software (Wegmüller et al., 2016). The images have been initially co-registered (aligned) to the dates Aug 08, 2018 (T015 A) and Aug 26, 2018 (T066D), respectively. Perpendicular baselines for all pairs are generally below 150 m, as expected for Sentinel-1 (see supplementary material). The topographic phase component was removed by considering the high-resolution digital elevation model provided by Swisstopo (SwissAlti3D), with a ground sampling distance of 5 m. The IPTA (Werner et al., 2003; Wegmüller et al., 2004) strategy was applied to retrieve average surface velocities and displacement time series for point targets with high temporal correlation (coherence). This method was proved effective both in flat regions (Stramondo et al., 2008; Strozzi et al., 2009) and alpine environments (Strozzi et al., 2017). Candidate point targets for the IPTA processing were selected based on a temporal mean-to-standard deviation ratio of the co-registered SAR intensity images exceeding 1.3, and a spectral correlation averaged over the single look complex stack greater than 0.4. Only candidates with a temporal correlation above 0.8 were considered in the subsequent processing steps. The reference point for both tracks is located at the total station Chatzulecher. Artefacts caused by vertical atmospheric stratification were estimated using a linear model as a function of topography and subsequently removed from each interferogram. After resolving the $2\pi$ phase ambiguity in the temporal domain (unwrapping), a two-dimensional linear regression was iteratively performed on the candidate point targets to estimate height and deformation rate. In the final stage, only points with a regression standard deviation below 1.3 rad were retained. The resulting point time series were filtered to mitigate atmospheric artifacts and other system noise sources (Wegmüller et al., 2021) using a triangular weighted average with a time window of 100 days. Lastly, a linear least-square spatial filtering was applied, considering neighboring targets within a 150 m radius. The final results include a total of 7148 and 7299 coherent point targets for the T015 A and T066D orbits and a total of 329 and 346 scenes, respectively.

The IPTA dataset is then corrected for the motion of the reference point by considering the cGNSS data measured at the Chatzulecher station (ALTS). Because the sampling from the satellite occurs every 6 d to 12 d depending on the number of available satellites, we first need to downsample the cGNSS data. A daily solution is calculated with respect to another cGNSS station (HOHT) situated in Rhone Valley. An intermediate reference station (FIES), closer to Chatzulecher, is also involved in this process to reduce the atmospheric noise on the GNSS positioning. More details on this procedure are available in Limpach et al. (2016). However, the daily signal from the cGNSS still includes noise (both instrumental and atmospheric), particularly in the vertical direction. To increase the signal-to-noise ratio further, we average the cGNSS position in the 6 d preceding a satellite observation (corresponding to the satellite's shortest observation window). Then, we calculate the projection of cGNSS station displacement to the SAR line of sight direction $d$:

$$d = cos(\theta)l_U - sin(\theta)cos(\alpha)l_N - sin(\theta)sin(\alpha)l_E \quad (1)$$

where $\theta$ is the satellite incidence angle (from vertical), $\alpha$ is the satellite flying direction (clockwise from North), and $l_U, l_N, l_E$ are, respectively, the Up, North, and East components of the GNSS position. Finally, the displacement of the reference point in the satellite's line of sight is added to the displacement observed from the SAR satellite.

### 2.2. Comparison between TS-InSAR, GNSS and RTS data

To test the validity of the results from the TS-InSAR processing, we benefit from the extensive ground monitoring system in place in the Aletsch valley (Oestreicher et al., 2021), and we compare cGNSS and RTS displacement timeseries converted in the LOS direction with nearby satellite points in a circular buffer around the stations. If the circle's radius is too small, only a few permanent scatterers (PSs) are retained, while if the radius is too large, the PSs have higher chances to experience different displacements than the displacement of the ground station. As a trade-off, we select a circle with a radius of 50 m (see Fig. 2 and the supplementary material). We find a good agreement between the three independent measurement methods. In particular, the long-term trends are well respected, and an extensive range of points exhibit seasonal patterns independently of the observation method. The comparison between TS-InSAR and cGNSS stations' displacement shows that the two methods give similar results regarding long-term trends and seasonal displacements. The number of PSs in 50 m circles around the cGNSS stations fluctuates from 0 to 20. In some cases (e.g., ALTS and ALTD in the ascending orbit), the displacement of the PSs deviates slightly from the one recorded by the cGNSS. Some of the deviations are due to the PS's location at a distance to the station and local changes of the surface displacement between the location of the station and the PSs, as sometimes local displacement variations are significant (Oestreicher et al., 2021).

One of the differences between the IPTA and ground-based displacement observations is the presence of larger noise in the satellite data in winter (Fig. 2). The snow covering the ground in winter introduces high variabilities in the phase values measured from the satellites. Instead of cutting out winter times from the analysis and/or the final displacement timeseries, we keep elevated noise in the data. The reason is that some points might stay uncovered for longer periods in winter, for example, on steep cliffs or close to springs where the flowing groundwater melts the snow earlier than at other places. South-oriented slopes and low-elevation areas also see a shorter snow-covered period during winter time. Those points stay coherent longer during the year and are important to retrieve information about annual cyclic displacement.

### 2.3. Statistical decomposition of satellite data

The PS displacement timeseries have likely been generated by multiple physical processes. For example, a point on a mountain slope might be subject to gravitational slope deformation, as well as thermoelastic and poroelastic effects. Moreover, system noise and atmospheric artifacts can also be present. All these signals are mixed in the satellite measurements and require disentanglement to gain more insight into the dominant slope processes. Statistical signal decomposition

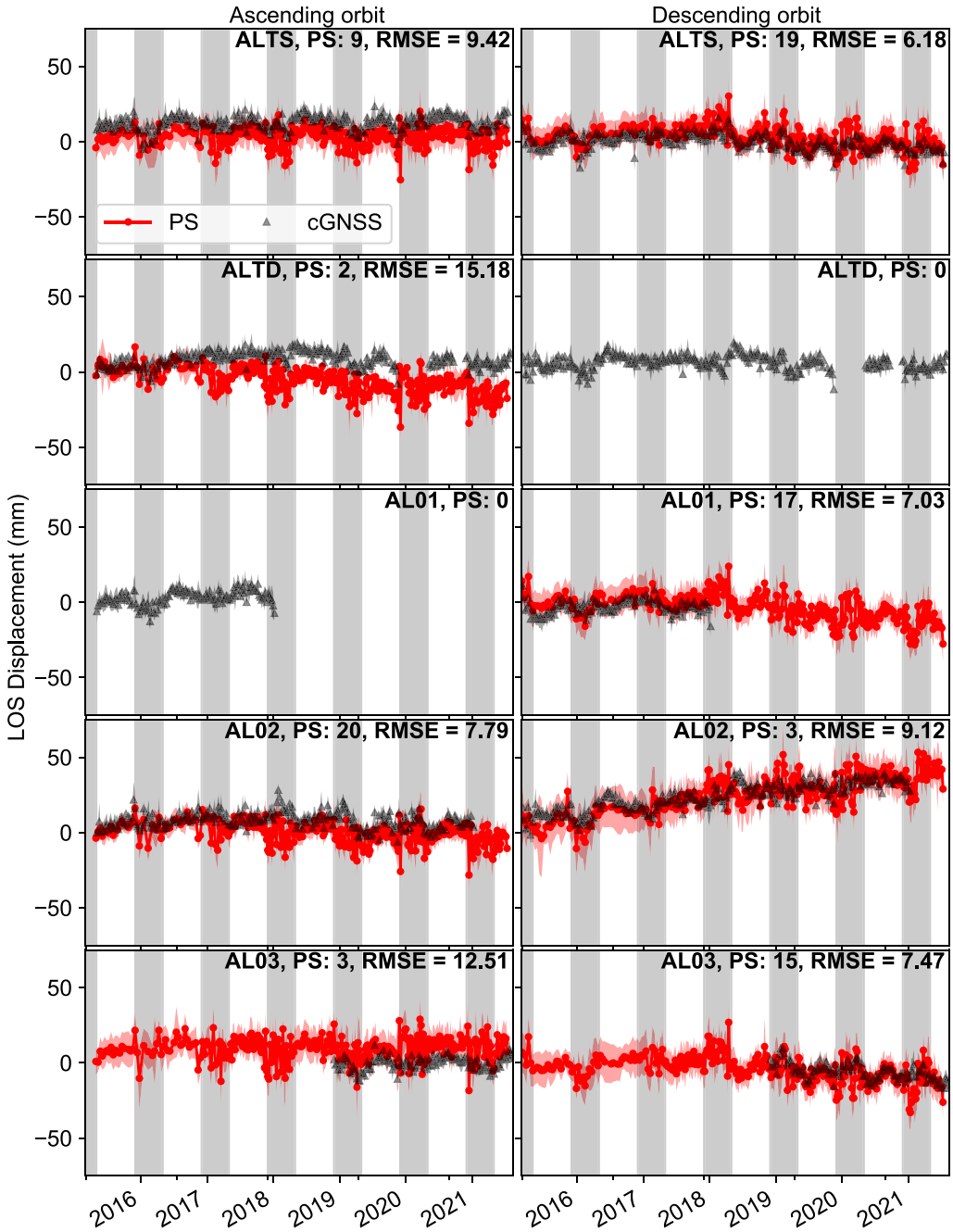


**Fig. 2.** Comparison between cGNSS stations displacement (dark grey) and nearby permanent scatterers (red) for the ascending (left) and descending (right) orbits in a circle of 50 m radius around each station. See Fig. 1 for the location of the five cGNSS stations. PS is the number of permanent scatterers in the 50 m circle around cGNSS stations, RMSE is in mm. Grey zones mark times when the stations are susceptible to being snow-covered (December to May), inducing a larger scattering of the satellite recordings. The point-by-point comparison for the total station's data is available in the supplementary material. (For interpretation of the references to color in this figure legend, the reader is referred to the web version of this article.)

techniques are commonly used to isolate parts of the signal from different sources (Gaddes et al., 2018). Among the available methods, the Principal Component Analysis (PCA) is a standard approach nowadays, but it often cannot correctly separate physical sources into different components. More advanced methods for blind source separation of TS-InSAR data include the Independent Component Analysis (ICA) (Ebmeier, 2016; Gaddes et al., 2018), and the variational Bayesian ICA (vbICA) (Gualandi and Liu, 2021), as well as deep learning autoencoders (Rouet-Leduc et al., 2021). The signal of interest extracted from the decomposition process consists of timeseries for each component at all permanent scatterers in the study area.

We use the vbICA, which statistically extracts Independent Components (ICs) from timeseries without a priori definition of the physical sources of the signal (Gualandi and Liu, 2021). Hereafter, we present the results of the vbICA in spatial mode (S-mode) with three ICs and whitening, meaning that the algorithm looks for independent components in the spatial domain, and the data has been sphered to allow for easier separation of almost parallel components. The variational Bayesian approach allows us to select the number of ICs following the Automatic Relevance Determination (ARD) method, as described by Choudrey and Roberts (2003), Gualandi and Liu (2021). We retain the smallest number of components where the ratio of maximum to minimum variance in the mixing matrix columns is below 0.01 (see

supplementary material). Additional components do not significantly add information and can be neglected (Gualandi and Liu, 2021).

## 3. Results

### 3.1. Location of Persistent Scatterers (PS) in the study area

Fig. 1 shows measurement points for ascending and descending orbits. Both datasets are referenced to a point where the relative displacement is known, located close to the center of the ~25 $km^2$ study area (Fig. 1). The reference point is relative to the reference cGNSS station HOHT, situated outside the study area in the Rhone Valley. HOHT records an additional uplift of 2.1 mm/yr relative to the Swiss coordinate reference system CHTRF2016 (Oestreicher et al., 2021). 7148 measurement points for the ascending orbit and 7299 for the descending one were analyzed. The points of the ascending orbit spread further away from the reference point, particularly on the North flank of the Rhone valley, around the villages of Riederalp and Bettmeralp (Fig. 1). For both datasets, no points are found on the glacier nor on the main part of the fast-moving Moosfluh landslide and small rock glacier East of AL03. This is because surface deformations in these regions are too rapid to ensure efficient tracking with the Sentinel 1 satellites, inducing decorrelation (Manconi et al., 2018; Manconi, 2021). The areas covered by forests (i.e., to the South-West of the Moosfluh instability) also lack points due to SAR signal decorrelation.

### 3.2. Irreversible displacements

The displacement time series over the 2015–2021 period are available for each measurement point in Fig. 1. We first extract the long-term trend in the displacement time series, revealing the irreversible deformation affecting the valley flanks (Fig. 3). The magnitude of the observed signal in the 6 yr dataset is up to 17 mm/yr in the descending orbit and around 8 mm/yr in the ascending orbit. The most significant surface velocities observed from the ascending and descending orbit take place at the main slope instabilities (Moosfluh, Driest, Riederalp-Bettmeralp) and on the South-East facing slopes at Ze Bächu (see Fig. 3).

The ascending and descending orbits show large velocities North-East of the Moosfluh instability. The descending orbit is particularly well suited to detect the landslide's motion, going to the North-West and down, hence away from the satellite line of sight (Glueer et al., 2020). While there are almost no PS in the central, faster part of the Moosfluh instability, PS on some parts of the landslide moving slower are preserved. The significant displacement away from the satellite in the descending orbit, in the slopes North-East of the Moosfluh landslide, induces a cluster of negative values in the histogram of LOS displacement (Figure S10 in the supplementary material). The detection of motion North-East of the Moosfluh instability is confirmed by the reflectors situated in this part of the slope (see supplementary material), which show a progressive attenuation of the deformation with the distance to the lateral scarps which formed in 2016 (Glueer et al., 2020). This could be explained by the field observation of decreasing openings of tension cracks with distance from the lateral scarp to the North-East (Truttmann et al., 2021; Hugentobler et al., 2021).

The Driest instability exhibits points moving away from and towards the satellite, respectively, for the top and bottom parts of the instability. This is consistent with RTS data and the rotational nature of this suspended rockslide (Vogler, 2015). The Riederalp-Bettmeralp deep-seated gravitational slope deformation area shows an average displacement rate of 1.1 mm/yr away from the satellite in the ascending orbit (1446 PS) and 0.7 mm/yr towards the satellite in the descending orbit (149 PS) (Fig. 3).

At other locations, for example, on the right flank of the valley along the glacier, significant long-term trends are detected and confirmed by cGNSS and RTS methods (see supplementary material). We observe displacement towards the valley center up to ~7 mm/yr on both valley flanks in the recently deglaciated bedrock slopes. No slope instabilities are mapped at this location, and no signs of instabilities are visible in the field.

### 3.3. Reversible deformation

The satellites detect seasonal cycles in deformation at an amplitude below the centimeter in the LOS direction (measured up to 3 cm by cGNSS). Such reversible motion is observed in large parts of the study area, with more substantial amplitudes in the vicinity of the glacier tongue (see Figure S11 in the supplementary material). The ascending and descending monthly timeseries of deformation weakly correlate with the variation of the hydraulic head (Pearson's correlation coefficient of respectively 0.47 and 0.22) measured in the borehole B4 (see Fig. 1). However, the deformation at the valley scale exhibits Pearson's correlation coefficients of respectively 0.57 and 0.62 with two months lag to the monitored hydraulic head (see Fig. 5) and even coefficients of 0.62 and 0.75 when discarding winter times. As the depth at which the hydraulic head is monitored in the borehole is relatively shallow (~45 m), the borehole hydraulic head reacts rapidly to the recharge of the fractured aquifer from the surface (Hugentobler et al., 2020).

By knowing the average direction of the groundwater-related displacement in the region from Oestreicher et al. (2021), we can combine the information from the ascending and descending orbits and estimate the displacement amplitude and orientation with the histograms (in the supplementary material). In Fig. 6, we jointly analyze the information derived from cGNSS, RTS, and TS-InSAR ascending and descending orbits along the two profiles shown in Fig. 4. The interpretation from the satellite displacement directions (red arrows) correlates well with the ones drawn from cGNSS and RTS observations (black arrows) performed in the South-East of the glacier. It complements these data for regions not covered by the other methods. Noteworthy, we found that the interpreted seasonal TS-InSAR displacement dynamics are generally underestimated compared to the ground-based observations (see Fig. 6). This bias might be due to different processes occurring locally, challenging the signal decomposition algorithm and leading to a cross-talk between the first and second ICs. It might likely originate from the TS-InSAR technique, which underestimates the ground deformation due to the orientation of the ascending and descending orbits and the lower signal-to-noise ratio of the ground observation network.

Our analysis with the vbICA method isolates a third independent displacement component in the study area (in the supplementary material). It shows a low magnitude of displacement, with only some points over 2 mm for the ascending orbit. The temporal pattern exhibits an annual cyclicity.

## 4. Discussion

One of the main advantages of TS-InSAR over ground-based studies is that the spatial sampling is substantially improved. While total stations are limited to their operational range and LOS from the station to reflectors, we could extend our analysis to a larger area with the satellites (Fig. 1), using a single reference point. Another significant advantage is that the method can be applied at other study sites without needing a large ground-based network and, retrospectively, thanks to satellite data archives. Fig. 2 shows that in some cases (e.g., AL01 and AL03 in the descending orbit), the IPTA method can fill a gap in the cGNSS timeseries. For example, some cGNSS stations have data interruptions: the station AL01 was destroyed by a snow avalanche in 2018 and replaced by AL03 at a safer location (Oestreicher et al., 2021). The ground displacement at these locations can be measured using satellites when the cGNSS stations are absent. We show good agreement between cGNSS, total station reflectors and TS-InSAR data despite the complex alpine environment and the presence of a glacier and slope instabilities in the middle of the study area (Fig. 2 and Figures

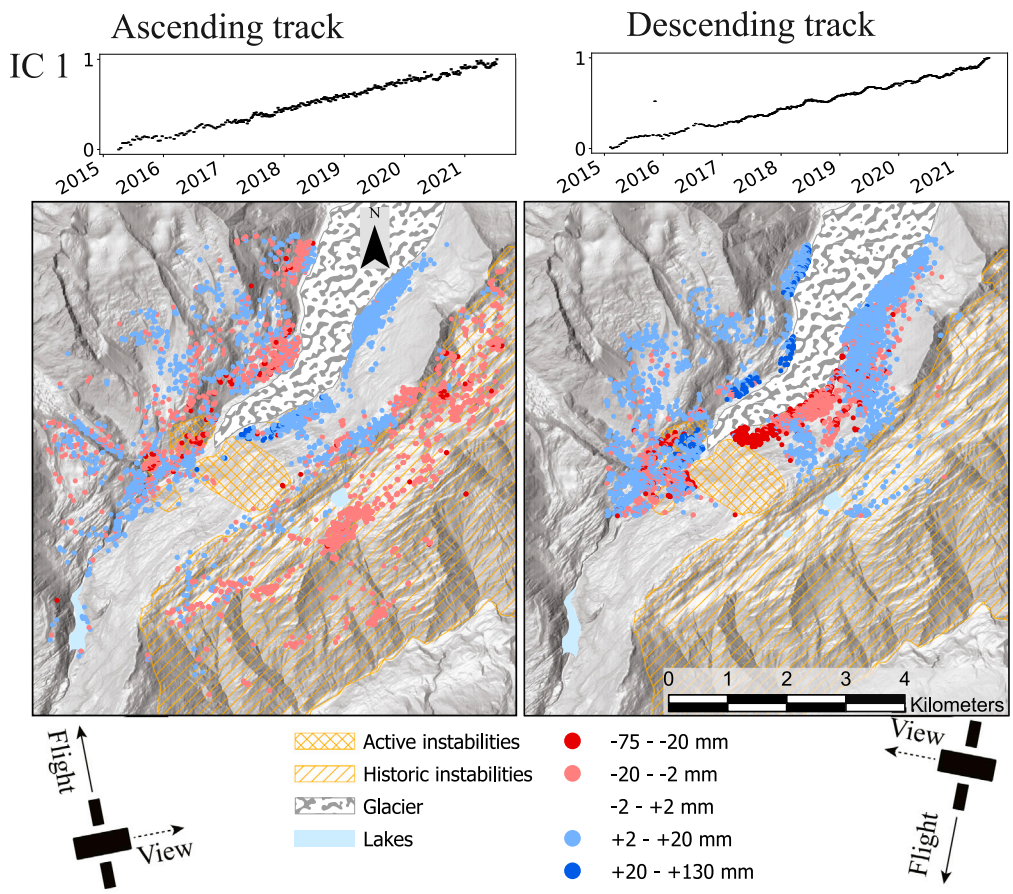


**Fig. 3.** First independent component of vbICA for the ascending and descending tracks of the satellite. The upper panels show the time series of the IC. The map displays displacement during the entire observation period. To reconstruct the displacement associated with the IC at a PS between two dates, multiply the value shown on the map by the difference in the time series of IC1 (upper panels) at the two given dates. Positive values (blue dots) on the map signify displacement towards the satellite as both time series display positive trends. (For interpretation of the references to color in this figure legend, the reader is referred to the web version of this article.)

in the supplementary information). Some exceptions are when no PS could be selected in the vicinity of the ground station for one of the satellite orbits due to geometric distortions.

Different statistical approaches exist to reduce the dimensionality of the dataset, including vbICA (Gualandi and Liu, 2021). A limitation of ICA is that it assumes non-moving sources. In some geophysical applications, this may be true, but it is not always the case. For example, the pore pressure anomaly responsible for the observed deformation can move during the recharge period (Oestreicher et al., 2023). The decomposition of the signal can still be performed, but a single physical source may be split into multiple independent components (ICs), with temporal functions being successive time derivatives of the original source time evolution (e.g., Larochelle et al., 2018; Michel et al., 2019). This is not the case in the studied area. Another limitation is the lack of guarantee of success: two sources may be not linearly combined, making the disentanglement of the sources too tricky for a linear approach like vbICA. Other complications may arise from noise in the TS-InSAR observations, particularly due to atmospheric effects in mountain environments. The vbICA has been previously successfully applied to GNSS position time series to study hydrologically induced deformation in the Alps (e.g., Serpelloni et al., 2018) and Himalayas (Larochelle et al., 2018). However, InSAR noise has its specific characteristics. ICA techniques have been used to study InSAR deformation time series in volcanic environments (e.g., Reddin et al., 2023; Amoruso et al., 2024), where topography plays an important role. While these studies have been mainly conducted to study large structures, we show a successful signal decomposition with the vbICA method at hill-slope scale in a complex alpine environment. Given the potential cross-talk between multiple ICs, possible future improvements may consider the integration of physical information within the blind source separation procedure. Our results, according to the Automatic Relevance Determination method (Gualandi and Liu, 2021), indicate the presence of three ICs. We note that the independent components are not guaranteed to correspond to physical processes. However, subsequent interpretation and comparison with environmental factors are required to interpret each independent component correctly (Gualandi and Liu, 2021).

The first IC is mainly composed of a linear trend, with a superimposed weak annual cyclic pattern (see Fig. 3). The linear trend is interpreted to be a long-term mechanical response of the slopes, and the superimposed, albeit smaller, seasonal signal might be a residual of the seasonal cycles identified in IC2, which is discussed later. At certain locations, the long-term trends are oriented downslope and represent the long-term gravitational slope motion. We do not only observe such slow surface displacements on mature landslides but also on slopes at early stages of damage accumulation. For example, we identify long-term gravitational slope motion close to the lateral boundaries of the Moosfluh and Driest instabilities (Glueer et al., 2019, 2020; Kos et al., 2016). Numerical experiments have shown that the Moosfluh and Driest instabilities are likely caused by glacier advance and retreat cycles that induce progressive damage in the surrounding slopes (Grämiger et al., 2017). Recent accelerations of the Moosfluh (Glueer et al., 2019) and Driest (Glueer et al., 2021) instabilities induce a non-linear displacement response of the slope that can be successfully decomposed by the vbICA method (Oestreicher et al., 2021). We note that the acceleration beyond the Sentinel-1 phase aliasing threshold cannot be retrieved with IPTA due to the intrinsic sampling limitations of the satellite SAR (Manconi, 2021). In addition, temperature (Grämiger et al., 2018;

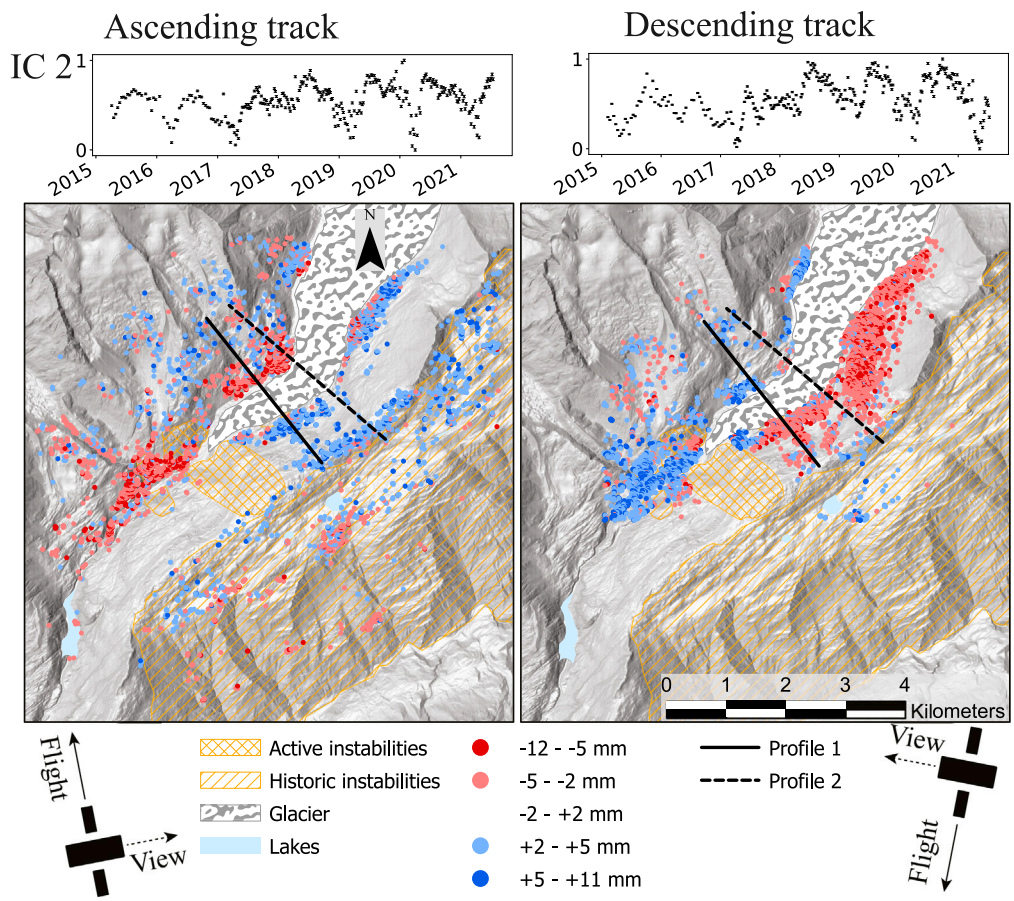


**Fig. 4.** Second independent component of vbICA exhibits cyclic annual displacement for the ascending and descending tracks of the satellite. The upper panels show the time series related to the IC. Positive values on the map signify displacement towards the satellite for a positive change in the time series, and values on the map display the maximum amplitude at each point. For example, red dots on the map represent locations where the ground moves away from the satellite when the timeseries goes up and towards it when the timeseries goes down.

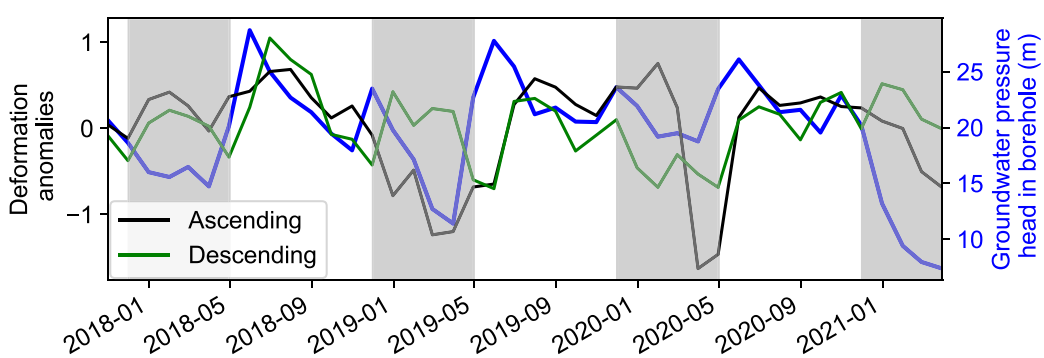


**Fig. 5.** Comparison between the monthly deformation anomalies (ascending orbit, black and descending orbit, green) and the monthly pressure head at B4 (blue). Grey areas are periods with expected partial snow coverage, during which lower correlation factors may be expected because of decorrelation induced by the snow. (For interpretation of the references to color in this figure legend, the reader is referred to the web version of this article.)

Hugentobler et al., 2021) and groundwater fluctuations (Grämiger et al., 2020; Hugentobler et al., 2022) have been identified as important factors contributing to the long-term damage of the slopes. The modeled damage is significantly greater when the temperature effect is taken into account (Grämiger et al., 2018), as rocks are rapidly exposed to warmer conditions (paraglacial thermal shock, Grämiger et al., 2018) and more short-term temperature fluctuations after the ice retreats (Hugentobler et al., 2021). With the contribution of annual groundwater table fluctuations, damage increases due to hydromechanical fatigue, and the mode of failure in the model resembles the landslide observations in the Aletsch Valley (Grämiger et al., 2020). The most substantial damage occurs directly at the glacier margin and moves up (or down) the slope with the pace of glacier retreat (or advance) during multiple glacial cycles (Hugentobler et al., 2022). We also observe significant long-term trends in the signal of PS located on a relict rock glacier to the east of the GNSS station AL03. In this case, it can be attributed to the long-term creep of the rock glacier (Marcer et al., 2021; Harris et al., 2009).

Because the analysis is based on two satellite orbits, we must reduce the dimensionality of the displacement data by making a hypothesis on the direction of displacement. For the long-term trends, we consider the direction parallel to the slope in Fig. 7, IC1. In slopes not influenced by

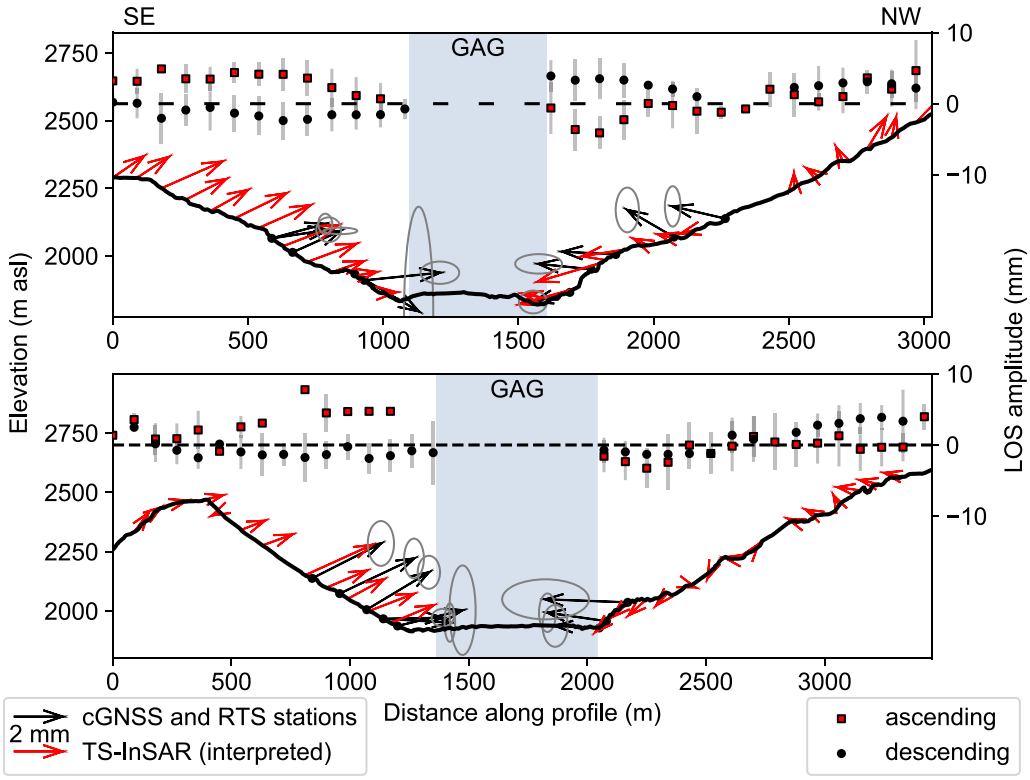


**Fig. 6.** Topographic profiles across the valley with IC2 displacement during spring to early summer. Top: profile 1; Bottom: profile 2 in Fig. 4. Black arrows are cGNSS and RTS data (grey ellipses for uncertainty). Red arrows are interpreted direction of ground displacement from TS-InSAR combining ascending and descending orbits, and points are raw data from Fig. 4 with a 90 m buffer distance around the profile. GAG stands for Great Aletsch Glacier, and its extent is delimited in blue. (For interpretation of the references to color in this figure legend, the reader is referred to the web version of this article.)

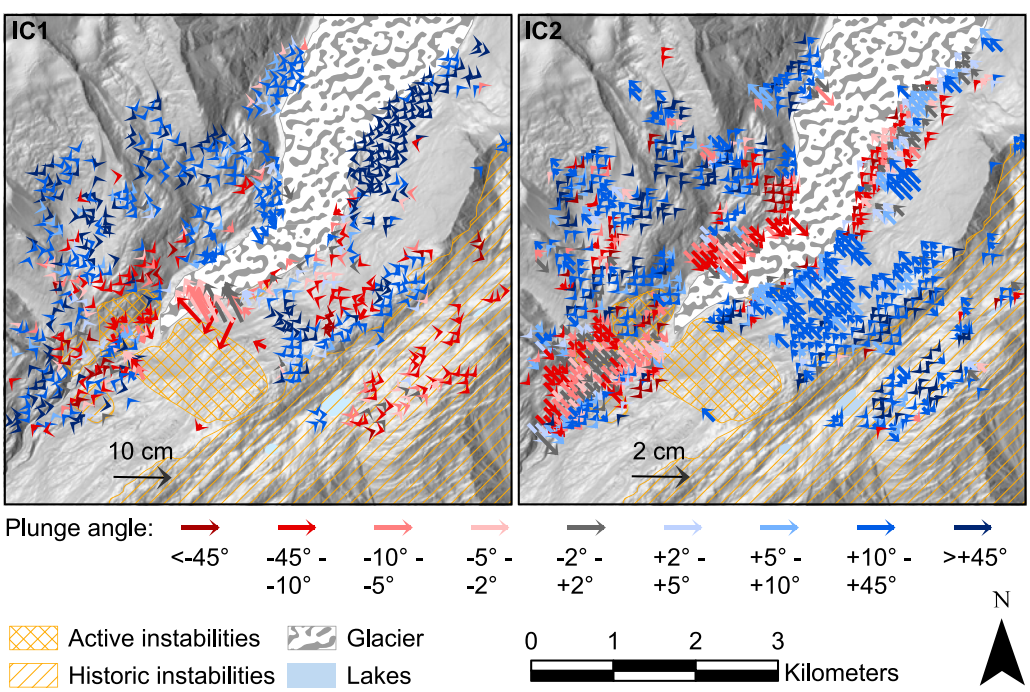


**Fig. 7.** Displacement obtained by combining the ascending and descending orbits with the local average slope direction for the first IC (left) and with the average dip direction of the foliation for the second IC (right) of the vbICA method. The arrows show the horizontal orientation of displacement and magnitude (the long-term trend for IC1, during recharge for IC2), and the colors display the plunge angle of the displacement.

significant gravitational movements, the signal decomposition reveals a minor uplift close to the current glacier margins (Fig. 7). This uplift is interpreted to be likely caused by the elastic isostatic rebound of the bedrock as a response to the contemporary glacier retreat (Hugentobler et al., 2022; Erfani Jazi et al., 2022). In the Ze Bächu region, the PS uplift is on average 2 mm/yr and up to 5 mm/yr. This uplift rate is confirmed by ground-truth measurements of nearby reflectors measured by the total station. In the Northeastern part of the study area, the

left flank of the glacier exhibits high plunge angles and uplift rates around 0.8 mm/yr to 1 mm/yr. The large horizontal motion recorded at Ze Bächu (average of 5.7 mm/yr for PS close to the glacier) and around the cGNSS stations AL03 and ALTS on the other valley flank is interpreted as partly caused by hydromechanical fatigue (Oestreicher et al., 2021). Other potential factors for these horizontal displacements could be a previously unidentified gravitational slope movement superimposed on a more substantial uplift than previously thought from the elastic rebound of the glacier removal or a horizontal component of the slope rebound from glacial debuttressing. The analysis of long-term trends shows that the study area is complex, including large displacements from slope isostatic rebound following the retreat of the glacier, gravitational slope deformations and hydromechanical fatigue processes that are often mingled. Newly identified locations with large gravitational displacements superposed on the glacial elastic rebound, North-East of the Driest instability, North-East of Chatzulecher, and North-East of the Moosfluh instability highlight zones with a potential to transition towards unstable slopes.

The second IC shows a reversible cyclic displacement. Such deformation dynamics have been previously identified with ground-based stations and attributed to pore pressure variations during groundwater recharge–discharge cycles (Dal Moro and Zadro, 1998; Lesparre et al., 2017; Serpelloni et al., 2018; Grillo et al., 2018; Braitenberg et al., 2019; Oestreicher et al., 2021). They are caused by changes in pore pressure in the rock mass linked to the strong seasonal dynamics of hydrologic cycles in alpine environments (Gleeson and Manning, 2008; Markovich et al., 2019; Somers and McKenzie, 2020). Indeed, at high elevations, groundwater recharge is mainly controlled by snowmelt in spring (Barnett et al., 2005; Manning et al., 2012), with a high magnitude of water table rise (de Palézieux and Loew, 2019). After recharge stops, groundwater is progressively discharged towards the receiving stream and springs network, associated with a decrease in the pore pressure (de Palézieux and Loew, 2019; Hugentobler et al., 2020). The natural pore pressure variations induce deformation of the valley slopes (Oestreicher et al., 2021; Chaussard and Farr, 2019). We constrain the displacement observed from the satellite in a vertical plane parallel to the average dip direction of the main alpine foliation (approximately 136° from N) in Fig. 7, IC2. Indeed, Oestreicher et al. (2021) showed that the displacement of cGNSS stations and total station reflectors in the valley was strongly influenced by the orientation of the alpine foliation. While the displacement in Spring is generally oriented upwards or horizontally out of the slope (see Fig. 7), downwards-oriented displacements or displacements toward the mountains are also found. Such signals are often situated at locations that also experience substantial linear displacements in IC1. The minor seasonal deformation contained in IC1 impacts the results of IC2, such that it erroneously identifies a signal in the opposite direction as compensation for the more significant amplitude signal of IC1. Such an intricate signal could also explain the discrepancies between the displacement recorded by the total station's reflectors and IC2 around the cGNSS station AL02 (see Fig. 6).

We interpret the third independent component with its low-magnitude displacement signal as a potential residual of the previously discussed groundwater-related motion or atmospheric noise in the satellite data. If attributed to pore pressure-induced deformation, this would indicate a non-stationary spatial pattern for the groundwater distribution. This can be the case, given the cross-talk between the first two ICs. Given the small amplitude of IC3, we cannot claim a physical origin for it with certainty. Another difficulty and source of noise in the area is the changing elevation around the glacier due to the ice removal. Further contributions from different environmental factors to surface displacements in the study area were evaluated, including statistical correlations, using GNSS stations and total station reflectors data and results are found in Oestreicher et al. (2021).

The slopes of the Aletsch Valley exhibit significant annual cyclic and reversible displacement, as observed at multiple observation points (Oestreicher et al., 2021). Three monitoring boreholes, drilled near the ice margins (at the time of the installation, Hugentobler et al., 2020), provide valuable data on pore pressure dynamics in the slope. All three are also equipped to track sub-millimetric deformation along the depth (~50 m) of the boreholes (Hugentobler et al., 2020). Hugentobler et al. (2021) observed that the shallower part of the slope responds primarily to variations in air temperature, while the deeper part of the ~50 m boreholes reacts more to the variations of groundwater and englacial pore pressure fluctuations, leading to reversible fracture scale deformation.

Fig. 5 compares borehole water pressure data with satellite-based slope displacements. It reveals a good temporal correlation, though with a slight time lag between the peak in the groundwater table and the peak in deformation observed from the satellite. This lag indicates a faster hydraulic response timescale of the shallower part of the aquifer compared to the slope-scale deformation measured from the satellite. In this environment, the hydraulic diffusivity of the near-surface part of the bedrock aquifer is higher than the one deeper (Welch and Allen, 2014; Roques et al., 2022). The denser, highly permeable fracture network near the surface facilitates quicker pressure diffusion and groundwater flow, while the deeper rock responds more slowly. Pore pressure changes in response to recharge may extend to depths of several hundred meters in alpine settings, beyond the borehole depth monitored here (Markovich et al., 2019; Moon et al., 2020; de Palézieux and Loew, 2019; Hugentobler, 2018; Oestreicher et al., 2021). Therefore, the delay observed in the deformation pattern is interpreted to be caused by the overall rock mass having a lower diffusivity and bulk permeability than the near-surface rocks, as hypothesized in previous studies (Oestreicher et al., 2021, 2023).

Numerical modeling experiments further support these observations, showing that surface deformation is strongly controlled by the fracture network characteristics, i.e. orientation, density, and length statistics (Oestreicher et al., 2023). In steep valley landforms, numerical models suggest that pore pressure-induced displacements are typically oriented horizontally or slightly downward near the valley center, while upslope points exhibit predominantly upward movements (Oestreicher et al., 2023), aligning with the observations presented here (see Figs. 6 and 7). We note that the hydromechanical fatigue that could result from strong cyclic pore pressure variations and associated slope deformations might induce increased irreversible deformation, as shown by Grämiger et al. (2020), Preisig et al. (2016), Eberhardt et al. (2016). As such, locations where IC2 is significant might experience larger damage and IC1 deformation in the future. Furthermore, the slopes near the glacier margins experience seasonal and daily temperature cycles for the first time since deglaciation, on top of the cyclic hydromechanical deformation (Hugentobler et al., 2021). They are subject to the combined effect of thermohydromechanical deformation and should be the focus of future studies.

## 5. Summary and conclusion

The ground displacements measured from TS-InSAR in the study area around the tongue of the Great Aletsch Glacier highlight the interplay of various physical sources of displacement signal. Using an advanced statistical approach, vbICA, we isolated three main independent components of displacement: a long-term trend, indicating irreversible displacement, and two annually reversible, cyclic displacement, with one being minor in amplitude and thus not interpreted here. We found that irreversible displacements are often driven by the creep of large rock instabilities and the slope's long-term response to the melting of the valley glacier. The slope's annual reversible displacement is caused by deep pore pressure changes in the slopes resulting from annual groundwater fluctuations.

The spatial variations in pore pressure-related surface deformation in the study area offer valuable insights into groundwater flow

processes within mountain slopes (Neely et al., 2021), which are often challenging to assess due to the remoteness of alpine environments (Hugentobler et al., 2020). Our results indicate that hydromechanically active structures in fractured bedrock aquifers respond to seasonal recharge–discharge cycles. Overall, we find good agreement between the displacement direction and magnitude captured by TS-InSAR, cGNSS and total stations (see Fig. 6 and Oestreicher et al., 2021), with the exception of locations displaying large amplitude in the long-term trend. The broader spatial coverage provided by TS-InSAR extends the analysis beyond the capabilities of traditional methods like cGNSS or total stations, allowing us to examine a larger portion of the slope. Our findings suggest that the hydrogeological response zone in the study area involves a large volume of the mountain slope, reaching a maximum depth of several hundred meters (Oestreicher et al., 2023).

We demonstrate the ability to isolate hydromechanical signals from satellite data in remote alpine regions around glaciers and large slope instabilities. Combining satellite data with ground-based measurements and coherent structural hypotheses opens up new possibilities for studying similarly remote and less instrumented regions.

## CRediT authorship contribution statement

**Nicolas Oestreicher:** Writing – review & editing, Writing – original draft, Visualization, Validation, Methodology, Investigation, Formal analysis, Conceptualization. **Andrea Manconi:** Writing – review & editing, Writing – original draft, Visualization, Validation, Supervision, Methodology, Investigation, Formal analysis. **Clément Roques:** Writing – review & editing, Visualization, Supervision, Formal analysis, Conceptualization. **Adriano Gualandi:** Writing – review & editing, Visualization, Validation, Methodology, Formal analysis. **Simon Loew:** Writing – review & editing, Visualization, Supervision, Resources, Project administration, Methodology, Funding acquisition, Data curation, Conceptualization.

## Funding sources

This work was supported by the Swiss National Science Foundation, Switzerland (project 172492).

## Declaration of competing interest

The authors declare that they have no known competing financial interests or personal relationships that could have appeared to influence the work reported in this paper.

## Acknowledgments

We thank GAMMA Remote Sensing AG for its significant help in the IPTA processing. We also thank Franziska Glueer, Marc Hugentobler, Reto Seifert, and the many field assistants who have contributed their time to this project. We thank colleagues and friends for their support. Finally, we thank the five reviewers, editor-in-chief, and associate editor for their constructive comments.

## Appendix A. Supplementary data

Supplementary material related to this article can be found online at https://doi.org/10.1016/j.rse.2025.114765.

## Data availability

The GNSS data used in this paper are available here: https://doi.org/10.3929/ethz-b-000563187. The TPS data are available here: https://doi.org/10.3929/ethz-b-000701944. The vbICA method code is available here: http://doi.org/10.5281/zenodo.4322548.

## References

Agliardi, F., Scuderi, M.M., Fusi, N., Collettini, C., 2020. Slow-to-fast transition of giant creeping rockslides modulated by undrained loading in basal shear zones. Nat. Commun. 11 (1), 1–11. http://dx.doi.org/10.1038/s41467-020-15093-3.

Ali, M.Z., Chu, H.J., Tatas, Burbey, T.J., 2022. Estimation of annual groundwater changes from insar-derived land subsidence. Water Environ. J. (March), 1–11. http://dx.doi.org/10.1111/wej.12802.

Amoruso, A., Gualandi, A., Crescentini, L., 2024. On the initial phase of the ongoing unrest at campi flegrei and its relation with subsidence at Vesuvio (Italy). Remote. Sens. 16, 1717. http://dx.doi.org/10.3390/RS16101717/S1, https://www.mdpi.com/2072-4292/16/10/1717/htm https://www.mdpi.com/2072-4292/16/10/1717.

Ballantyne, C.K., Wilson, P., Gheorghiu, D., Rodés, A., 2014. Enhanced rock-slope failure following ice-sheet deglaciation: timing and causes. Earth Surf. Process. Landf. 39 (7), 900–913. http://dx.doi.org/10.1002/esp.3495.

Barnett, T.P., Adam, J.C., Lettenmaier, D.P., 2005. Potential impacts of a warming climate on water availability in snow-dominated regions. Nature 438 (7066), 303–309. http://dx.doi.org/10.1038/nature04141.

Béjar-Pizarro, M., Ezquerro, P., Herrera, G., Tomás, R., Guardiola-Albert, C., Ruiz Hernández, J.M., Fernández Merodo, J.A., Marchamalo, M., Martínez, R., 2017. Mapping groundwater level and aquifer storage variations from InSAR measurements in the Madrid aquifer, Central Spain. J. Hydrol. 547, 678–689. http://dx.doi.org/10.1016/j.jhydrol.2017.02.011.

Berger, A., Mercolli, I., Herwegh, M., Gnos, E., 2016. Geological Map of the Aar Massif, Tavetsch and Gotthard Nappes. - Geol. spec. Map 1:100000, map sheet 129.

Bock, Y., Agnew, D.C., Fang, P., Genrich, J.F., Hager, B.H., Herring, T.A., Hudnut, K.W., King, R.W., Larsen, S., Minster, J.B., Stark, K., Wdowinski, S., Wyatt, F.K., 1993. Detection of crustal deformation from the landers earthquake sequence using continuous geodetic measurements. Nature 361 (6410), 337–340. http://dx.doi.org/10.1038/361337a0.

Braitenberg, C., Pivetta, T., Barbolla, D.F., Gabrovšek, F., Devoti, R., Nagy, I., 2019. Terrain uplift due to natural hydrologic overpressure in karstic conduits. Sci. Rep. 9 (1), 3934. http://dx.doi.org/10.1038/s41598-019-38814-1.

Chaussard, E., Farr, T.G., 2019. A new method for isolating elastic from inelastic deformation in aquifer systems: Application to the San Joaquin Valley, CA. Geophys. Res. Lett. 46 (19), 10800–10809. http://dx.doi.org/10.1029/2019GL084418.

Chen, F., Lin, H., Li, Z., Chen, Q., Zhou, J., 2012. Interaction between permafrost and infrastructure along the Qinghai–Tibet Railway detected via jointly analysis of C- and L-band small baseline SAR interferometry. Remote Sens. Environ. 123, 532–540. http://dx.doi.org/10.1016/J.RSE.2012.04.020.

Chen, H., Zhao, C., Tomás, R., Reyes-Carmona, C., Kang, Y., 2025. Integrating InSAR and non-rigid optical pixel offsets to explore the kinematic behaviors of the lanuza complex landslide. Remote Sens. Environ. 320, 114651. http://dx.doi.org/10.1016/J.RSE.2025.114651.

Choudrey, R.A., Roberts, S.J., 2003. Variational mixture of Bayesian independent component analyzers. Neural Comput. 15 (1), 213–252. http://dx.doi.org/10.1162/089976603321043766.

Collins, B.D., Stock, G.M., Eppes, M.C., Lewis, S.W., Corbett, S.C., Smith, J.B., 2018. Thermal influences on spontaneous rock dome exfoliation. Nat. Commun. 9 (1), 1–12. http://dx.doi.org/10.1038/s41467-017-02728-1.

Crosetto, M., Monserrat, O., Cuevas-González, M., Devanthéry, N., Crippa, B., 2016. Persistent scatterer interferometry: A review. ISPRS J. Photogramm. Remote Sens. 115, 78–89. http://dx.doi.org/10.1016/J.ISPRSJPRS.2015.10.011.

Dal Moro, G., Zadro, M., 1998. Subsurface deformations induced by rainfall and atmospheric pressure: Tilt/strain measurements in the NE-Italy seismic area. Earth Planet. Sci. Lett. http://dx.doi.org/10.1016/S0012-821X(98)00203-9.

de Palézieux, L., Loew, S., 2019. Long-term transient groundwater pressure and deep infiltration in alpine mountain slopes (Poschiavo Valley, Switzerland). Hydrogeol. J. 27 (8), 2817–2834. http://dx.doi.org/10.1007/s10040-019-02025-9.

Dufour, G.H., 1865. Schlussbericht des Herrn General Dufour über die topographische Karte der Schweiz. Bundesblatt 1 (10), 203–216.

Eberhardt, E., Preisig, G., Gischig, V., 2016. Progressive failure in deep-seated rockslides due to seasonal fluctuations in pore pressures and rock mass fatigue. In: Aversa, S., Cascini, L., Picarelli, L., Scavia, C. (Eds.), Landslides and Engineered Slopes. Experience, Theory and Practice, Proceeding CRC Press, London, p. 16.

Ebmeier, S.K., 2016. Application of independent component analysis to multitemporal insar data with volcanic case studies. J. Geophys. Res.: Solid Earth 121 (12), 8970–8986. http://dx.doi.org/10.1002/2016JB013765.

Erfani Jazi, Z., Motagh, M., Klemann, V., 2022. Inferring mass loss by measuring contemporaneous deformation around the Helheim Glacier, Southeastern Greenland, Using Sentinel-1 insar. Remote. Sens. 14 (16), 3956. http://dx.doi.org/10.3390/rs14163956.

Federal Office of Topography swisstopo, 2024. Swisstopo.

Frukacz, M., Presl, R., Wieser, A., Favot, D., 2017. Pushing the sensitivity limits of RTS-based continuous deformation monitoring of an alpine valley. Appl. Geomatics 9 (2), 81–92. http://dx.doi.org/10.1007/s12518-017-0182-2.

Gaddes, M.E., Hooper, A., Bagnardi, M., Inman, H., Albino, F., 2018. Blind signal separation methods for InSAR: The potential to automatically detect and monitor signals of volcanic deformation. J. Geophys. Res.: Solid Earth 123 (11), 10226–10251. http://dx.doi.org/10.1029/2018JB016210.

GLAMOS - Glacier Monitoring Switzerland, 2021. Swiss Glacier Length Change (release 2021).

Gleeson, T., Manning, A.H., 2008. Regional groundwater flow in mountainous terrain: Three-dimensional simulations of topographic and hydrogeologic controls. Water Resour. Res. 44 (10), http://dx.doi.org/10.1029/2008WR006848.

Glueer, F., Loew, S., Manconi, A., 2020. Paraglacial history and structure of the moosfluh landslide (1850–2016), Switzerland. Geomorphology 355, 106677. http://dx.doi.org/10.1016/j.geomorph.2019.02.021.

Glueer, F., Loew, S., Manconi, A., Aaron, J., 2019. From toppling to sliding: Progressive evolution of the Moosfluh Landslide, Switzerland. J. Geophys. Res.: Earth Surf. 124 (12), 2899–2919. http://dx.doi.org/10.1029/2019JF005019.

Glueer, F., Loew, S., Seifert, R., Aaron, J., Grämiger, L., Conzett, S., Limpach, P., Wieser, A., Manconi, A., 2021. Robotic total station monitoring in high alpine paraglacial environments: Challenges and solutions from the Great Aletsch Region (Valais, Switzerland). Geosciences 11 (11), 471. http://dx.doi.org/10.3390/geosciences11110471.

Grämiger, L.M., Moore, J.R., Gischig, V.S., Ivy-Ochs, S., Loew, S., 2017. Beyond debuttressing: Mechanics of paraglacial rock slope damage during repeat glacial cycles. J. Geophys. Res.: Earth Surf. 122 (4), 1004–1036. http://dx.doi.org/10.1002/2016JF003967.

Grämiger, L.M., Moore, J.R., Gischig, V.S., Loew, S., 2018. Thermomechanical stresses drive damage of alpine valley rock walls during repeat glacial cycles. J. Geophys. Res.: Earth Surf. 123 (10), 2620–2646. http://dx.doi.org/10.1029/2018JF004626.

Grämiger, L.M., Moore, J.R., Gischig, V.S., Loew, S., Funk, M., Limpach, P., 2020. Hydromechanical rock slope damage during late pleistocene and holocene glacial cycles in an alpine valley. J. Geophys. Res.: Earth Surf. 125 (8), 1–24. http://dx.doi.org/10.1029/2019JF005494.

Grillo, B., Braitenberg, C., Nagy, I., Devoti, R., Zuliani, D., Fabris, P., 2018. Cansiglio karst plateau: 10 years of geodetic-hydrological observations in seismically active Northeast Italy. Pure Appl. Geophys. 175 (5), 1765–1781. http://dx.doi.org/10.1007/s00024-018-1860-7.

Gualandi, A., Liu, Z., 2021. Variational Bayesian independent component analysis for InSAR displacement time-series with application to Central California, USA. J. Geophys. Res.: Solid Earth 126 (4), http://dx.doi.org/10.1029/2020JB020845.

Harris, C., Arenson, L.U., Christiansen, H.H., Etzelmüller, B., Frauenfelder, R., Gruber, S., Haeberli, W., Hauck, C., Hölzle, M., Humlum, O., Isaksen, K., Kääb, A., Kern-Lütschg, M.A., Lehning, M., Matsuoka, N., Murton, J.B., Nötzli, J., Phillips, M., Ross, N., Seppälä, M., Springman, S.M., Vonder Mühll, D., 2009. Permafrost and climate in Europe: Monitoring and modelling thermal, geomorphological and geotechnical responses. Earth-Sci. Rev. 92, 117–171. http://dx.doi.org/10.1016/J.EARSCIREV.2008.12.002.

Hugentobler, M., 2018. High-Resolution Monitoring and Analysis of Sub- Surface Rock Slope Deformation in a Deglaciating Environment (Aletsch Valley , Switzerland). Technical Report, ETH Zurich, p. 28.

Hugentobler, M., Aaron, J., Loew, S., 2021. Rock slope temperature evolution and micrometer-scale deformation at a retreating glacier margin. J. Geophys. Res.: Earth Surf. 126 (11), 1–33. http://dx.doi.org/10.1029/2021JF006195.

Hugentobler, M., Aaron, J., Loew, S., Roques, C., 2022. Hydro-mechanical interactions of a rock slope with a retreating temperate valley glacier. J. Geophys. Res.: Earth Surf. 127 (4), http://dx.doi.org/10.1029/2021JF006484.

Hugentobler, M., Loew, S., Aaron, J., Roques, C., Oestreicher, N., 2020. Borehole monitoring of thermo-hydro-mechanical rock slope processes adjacent to an actively retreating glacier. Geomorphology 362, 107190. http://dx.doi.org/10.1016/j.geomorph.2020.107190.

Huss, M., Hock, R., 2018. Global-scale hydrological response to future glacier mass loss. Nat. Clim. Chang. 8 (2), 135–140. http://dx.doi.org/10.1038/s41558-017-0049-x.

Kos, A., Amann, F., Strozzi, T., Delaloye, R., von Ruette, J., Springman, S., 2016. Contemporary glacier retreat triggers a rapid landslide response, Great Aletsch Glacier, Switzerland. Geophys. Res. Lett. http://dx.doi.org/10.1002/2016GL071708.

Larochelle, S., Gualandi, A., Chanard, K., Avouac, J.P., 2018. Identification and extraction of seasonal geodetic signals due to surface load variations. J. Geophys. Res.: Solid Earth http://dx.doi.org/10.1029/2018JB016607.

Lesparre, N., Boudin, F., Champollion, C., Chéry, J., Danquigny, C., Seat, H.C., Cattoen, M., Lizion, F., Longuevergne, L., 2017. New insights on fractures deformation from tiltmeter data measured inside the Fontaine de Vaucluse karst system. Geophys. J. Int. http://dx.doi.org/10.1093/gji/ggw446.

Limpach, P., Geiger, A., Raetzo, H., 2016. GNSS for deformation and geohazard monitoring in the swiss alps. In: Proceedings of the 3rd Joint International Symposium on Deformation Monitoring, no. 1, pp. 1–4.

Loew, S., Ebneter, F., Bremen, R., Herfort, M., Lützenkirchen, V., Matousek, F., 2007. Annual opening and closure of Alpine Valleys. Felsbau : Rock Soil Eng. 25 (5), 1–60.

Manconi, A., 2021. How phase aliasing limits systematic space-borne DInSAR monitoring and failure forecast of alpine landslides. Eng. Geol. 287, http://dx.doi.org/10.1016/J.ENGGEO.2021.106094.

Manconi, A., Jones, N., Loew, S., Strozzi, T., Caduff, R., Wegmueller, U., 2024. Monitoring surface deformation with spaceborne radar interferometry in landslide complexes: insights from the Brienz/Brinzauls slope instability, Swiss Alps. Landslides 21, 2519–2533. http://dx.doi.org/10.1007/S10346-024-02291-Z/FIGURES/8.

Manconi, A., Kourkouli, P., Caduff, R., Strozzi, T., Loew, S., 2018. Monitoring surface deformation over a failing rock slope with the ESA sentinels: Insights from Moosfluh instability, Swiss Alps. Remote. Sens. 10 (5), http://dx.doi.org/10.3390/rs10050672.

Manning, A.H., Clark, J.F., Diaz, S.H., Rademacher, L.K., Earman, S., Niel Plummer, L., 2012. Evolution of groundwater age in a mountain watershed over a period of thirteen years. J. Hydrol. http://dx.doi.org/10.1016/j.jhydrol.2012.06.030.

Marcer, M., Cicoira, A., Cusicanqui, D., Bodin, X., Echelard, T., Obregon, R., Schoeneich, P., 2021. Rock glaciers throughout the french alps accelerated and destabilised since 1990 as air temperatures increased. Commun. Earth Environ. 2 (1), http://dx.doi.org/10.1038/s43247-021-00150-6.

Markovich, K.H., Manning, A.H., Condon, L.E., McIntosh, J.C., 2019. Mountain-block recharge: A review of current understanding. Water Resour. Res. http://dx.doi.org/10.1029/2019WR025676.

Mey, J., Scherler, D., Wickert, A.D., Egholm, D.L., Tesauro, M., Schildgen, T.F., Strecker, M.R., 2016. Glacial isostatic uplift of the European Alps. Nat. Commun. 7 (1), 13382. http://dx.doi.org/10.1038/ncomms13382.

Michel, S., Gualandi, A., Avouac, J.P., 2019. Interseismic coupling and slow slip events on the cascadia megathrust. Pure Appl. Geophys. 176, 3867–3891. http://dx.doi.org/10.1007/S00024-018-1991-X/FIGURES/12.

Moon, S., Perron, J.T., Martel, S.J., Goodfellow, B.W., Mas Ivars, D., Hall, A., Heyman, J., Munier, R., Näslund, J.-O., Simeonov, A., Stroeven, A.P., 2020. Present-day stress field influences bedrock fracture openness deep into the subsurface. Geophys. Res. Lett. 47 (23), http://dx.doi.org/10.1029/2020GL090581.

Neely, W.R., Borsa, A.A., Burney, J.A., Levy, M.C., Silverii, F., Sneed, M., 2021. Characterization of groundwater recharge and flow in california's san joaquin valley from InSAR-observed surface deformation. Water Resour. Res. 57 (4), http://dx.doi.org/10.1029/2020WR028451.

Oestreicher, N., Lei, Q., Loew, S., Roques, C., 2023. Bedrock fractures control groundwater-driven mountain slope deformations. J. Geophys. Res.: Earth Surf. 128 (11), http://dx.doi.org/10.1029/2022JF006885.

Oestreicher, N., Loew, S., Roques, C., Aaron, J., Gualandi, A., Longuevergne, L., Limpach, P., Hugentobler, M., 2021. Controls on spatial and temporal patterns of slope deformation in an Alpine Valley. J. Geophys. Res.: Earth Surf. 126 (12), http://dx.doi.org/10.1029/2021jf006353.

Oliva, M., Mercier, D., Ruiz-Fernández, J., McColl, S., 2020. Paraglacial processes in recently deglaciated environments. Land Degrad. Dev. 31 (15), 1871–1876. http://dx.doi.org/10.1002/ldr.3283.

Preisig, G., Eberhardt, E., Smithyman, M., Preh, A., Bonzanigo, L., 2016. Hydromechanical rock mass fatigue in deep-seated landslides accompanying seasonal variations in pore pressures. Rock Mech. Rock Eng. 49 (6), 2333–2351. http://dx.doi.org/10.1007/s00603-016-0912-5.

Reddin, E., Ebmeier, S.K., Rivalta, E., Bagnardi, M., Baker, S., Bell, A.F., Mothes, P., Aguaiza, S., 2023. Magmatic connectivity among six galápagos volcanoes revealed by satellite geodesy. Nat. Commun. 14 (1), 1–11. http://dx.doi.org/10.1038/s41467-023-42157-x.

Roques, C., Rupp, D.E., De Dreuzy, J.R., Longuevergne, L., Jachens, E.R., Grant, G., Aquilina, L., Selker, J.S., 2022. Recession discharge from compartmentalized bedrock hillslopes. Hydrol. Earth Syst. Sci. 26 (16), 4391–4405. http://dx.doi.org/10.5194/hess-26-4391-2022.

Rosen, P., Hensley, S., Joughin, I., Li, F., Madsen, S., Rodriguez, E., Goldstein, R., 2000. Synthetic aperture radar interferometry. Proc. IEEE 88 (3), 333–382. http://dx.doi.org/10.1109/5.838084.

Rouet-Leduc, B., Jolivet, R., Dalaison, M., Johnson, P.A., Hulbert, C., 2021. Autonomous extraction of millimeter-scale deformation in InSAR time series using deep learning. Nat. Commun. 12 (1), 6480. http://dx.doi.org/10.1038/s41467-021-26254-3.

Serpelloni, E., Pintori, F., Gualandi, A., Scoccimarro, E., Cavaliere, A., Anderlini, L., Belardinelli, M.E., Todesco, M., 2018. Hydrologically induced karst deformation: Insights from GPS measurements in the Adria-Eurasia Plate Boundary Zone. J. Geophys. Res.: Solid Earth http://dx.doi.org/10.1002/2017JB015252.

Somers, L.D., McKenzie, J.M., 2020. A review of groundwater in high mountain environments. Wiley Interdiscip. Rev.: Water 7 (6), 1–27. http://dx.doi.org/10.1002/wat2.1475.

Song, S., Bai, L., Yang, C., 2022. Characterization of the land deformation induced by groundwater withdrawal and aquifer parameters using InSAR observations in the Xingtai Plain, China. Remote. Sens. 14 (18), 4488. http://dx.doi.org/10.3390/rs14184488.

Sternai, P., Sue, C., Husson, L., Serpelloni, E., Becker, T.W., Willett, S.D., Faccenna, C., Di Giulio, A., Spada, G., Jolivet, L., Valla, P., Petit, C., Nocquet, J.M., Walpersdorf, A., Castelltort, S., 2019. Present-day uplift of the European Alps: Evaluating mechanisms and models of their relative contributions. Earth-Sci. Rev. 190, 589–604. http://dx.doi.org/10.1016/j.earscirev.2019.01.005.

Storni, E., Hugentobler, M., Manconi, A., Loew, S., 2020. Geomorphology monitoring and analysis of active rockslide-glacier interactions (Moosfluh , Switzerland ). Geomorphology 371, 107414. http://dx.doi.org/10.1016/j.geomorph.2020.107414.

Stramondo, S., Bozzano, F., Marra, F., Wegmuller, U., Cinti, F.R., Moro, M., Saroli, M., 2008. Subsidence induced by urbanisation in the city of Rome detected by advanced InSAR technique and geotechnical investigations. Remote Sens. Environ. 112, 3160–3172. http://dx.doi.org/10.1016/J.RSE.2008.03.008.

Strozzi, T., Caduff, R., Wegmüller, U., Raetzo, H., Hauser, M., 2017. Widespread surface subsidence measured with satellite SAR interferometry in the Swiss alpine range associated with the construction of the Gotthard Base Tunnel. Remote Sens. Environ. 190, 1–12. http://dx.doi.org/10.1016/j.rse.2016.12.007.

Strozzi, T., Delaloye, R., Kääb, A., Ambrosi, C., Perruchoud, E., Wegmüller, U., 2010. Combined observations of rock mass movements using satellite SAR interferometry, differential GPS, airborne digital photogrammetry, and airborne photography interpretation. J. Geophys. Res.: Earth Surf. http://dx.doi.org/10.1029/2009JF001311.

Strozzi, T., Teatini, P., Tosi, L., 2009. TerraSAR-X reveals the impact of the mobile barrier works on venice coastland stability. Remote Sens. Environ. 113, 2682–2688. http://dx.doi.org/10.1016/J.RSE.2009.08.001.

Torres, R., Snoeij, P., Geudtner, D., Bibby, D., Davidson, M., Attema, E., Potin, P., Rommen, B., Floury, N., Brown, M., Traver, I.N., Deghaye, P., Duesmann, B., Rosich, B., Miranda, N., Bruno, C., L'Abbate, M., Croci, R., Pietropaolo, A., Huchler, M., Rostan, F., 2012. GMES sentinel-1 mission. Remote Sens. Environ. 120, 9–24. http://dx.doi.org/10.1016/J.RSE.2011.05.028.

Truttmann, S., Herwegh, M., Schreurs, G., Ebert, A., Hardmeier, S., 2021. The effect of pre-existing structures on the Moosfluh landslide and its lateral propagation (Great Aletsch Glacier, Switzerland). Geomorphology 377, 107530. http://dx.doi.org/10.1016/j.geomorph.2020.107530.

Vasco, D.W., Farr, T.G., Jeanne, P., Doughty, C., Nico, P., 2019. Satellite-based monitoring of groundwater depletion in California's Central Valley. Sci. Rep. 9 (1), 1–14. http://dx.doi.org/10.1038/s41598-019-52371-7.

Vogler, M., 2015. Hydro-mechanical interactions between the great aletsch glacier and the Driest landslide (Switzerland).

Wasowski, J., Bovenga, F., 2014. Investigating landslides and unstable slopes with satellite Multi temporal interferometry: Current issues and future perspectives. Eng. Geol. 174, 103–138. http://dx.doi.org/10.1016/J.ENGGEO.2014.03.003.

Wegmüller, U., Magnard, C., Werner, C., Strozzi, T., Caduff, R., Manconi, A., 2021. Methods to avoid being affected by non-zero closure phase in InSAR time series analysis in a multi-reference stack. Procedia Comput. Sci. 181, 511–518. http://dx.doi.org/10.1016/J.PROCS.2021.01.197.

Wegmüller, U., Werner, C., Strozzi, T., Wiesmann, A., 2004. Multi-temporal interferometric point target analysis. In: Analysis of Multi-Temporal Remote Sensing Images. World Scientific, pp. 136–144. http://dx.doi.org/10.1142/9789812702630_0015.

Wegmüller, U., Werner, C., Strozzi, T., Wiesmann, A., Frey, O., Santoro, M., 2016. Sentinel-1 support in the GAMMA software. Procedia Comput. Sci. 100, 1305–1312. http://dx.doi.org/10.1016/j.procs.2016.09.246.

Welch, L.A., Allen, D.M., 2014. Hydraulic conductivity characteristics in mountains and implications for conceptualizing bedrock groundwater flow. Hydrogeol. J. 22 (5), 1003–1026. http://dx.doi.org/10.1007/s10040-014-1121-5.

Werner, C., Wegmüller, U., Strozzi, T., Wiesmann, A., 2003. Interferometric point target analysis for deformation mapping. Int. Geosci. Remote. Sens. Symp. (IGARSS) 7 (C), 4362–4364. http://dx.doi.org/10.1109/igarss.2003.1295516.